Earthq Eng & Eng Vib (2023) 22: 747-762 **DOI**: https://doi.org/10.1007/s11803-023-2196-6

Hysteretic behavior of post-tensioned precast segmental CFT double-column piers

Li Xian[1, 2†], Zhang Zilin[1‡], Zhou Tao[1‡], Xiao Yu[1, 3‡] and Sun Yushun[1§]

1. *Jiangsu Key Laboratory of Environmental Impact and Structural Safety in Civil Engineering, China University of Mining and Technology, Xuzhou 221116, China*
2. *Jiangsu Collaborative Innovation Center for Building Energy Saving and Construction Technology, Xuzhou 221116, China*
3. *School of Transportation, Southeast University, Nanjing 211189, China*

Abstract: Considering the desirable behavior of concrete filled steel tube (CFT) columns and the complicated behavior of segmental double-column piers under cyclic loads, three post-tensioned precast segmental CFT double-column pier specimens were tested to extend their application in moderate and high seismicity areas. The effects of the number of CFT segments and the steel endplates as energy dissipaters on the seismic behavior of the piers were evaluated. The experimental results show that the segmental piers exhibited stable hysteretic behavior with small residual displacements under cyclic loads. All the tested specimens achieved a drift ratio no less than 13% without significant damage and strength deterioration due to the desirable behavior of CFT columns. Since the deformation of segmental columns was mainly concentrated at the column-footing interfaces, the increase of the segment numbers for each column had no obvious effects on the loading capacity but reduced the initial stiffness of the specimens. The use of steel endplates improved the bearing capacity, stiffness and energy dissipation of segmental piers, but weakened their self-centering capacity. Fiber models were also proposed to simulate the hysteretic behavior of the tested specimens, and the influences of segment numbers and prestress levels on seismic behavior were further studied.

Keywords: precast segmental piers; cyclic loading test; seismic behavior; concrete filled tube column; rockinganalysis

1 Introduction

Previous earthquakes have demonstrated that bridge piers designed according to the current ductile method are prone to suffer irreparable structural damage and inevitable residual deformations under strong earthquakes due to the forming of plastic hinges at pier bases (Han *et al.*, 2009; Schexnayder *et al.*, 2014). These damage and residual deformations lead to long-term closure of highways while high-cost retrofits or even complete replacements are carried out after an earthquake. For example, after the 1995 Kobe earthquake in Japan, more than 100 reinforced concrete piers were demolished due to too large post-earthquake residual drift angles over 1.5% (Takada *et al.*, 1995; Lee and Billington, 2010). Therefore, recent research efforts have been aligned at developing bridge technologies to reduce the post-earthquake residual deformation and to accelerate the recovery of traffic after a seismic event. The concept of pier rocking therefore has attracted more attention in recent years.

Post-tensioned precast segmental piers, with the advantages of both rocking piers and accelerated bridge construction, are becoming a promising pier type and have been used in bridge construction projects in regions of low seismicity (Billington *et al*., 1999; Transportation Research Board, 2003). For post-tensioned precast segmental piers, the segments are prefabricated in the factory, and then, in the field, they are stacked on top of each other and connected using unbonded post-tensioning tendons passing through ducts cast in the segments. Under a strong earthquake, the piers will rock back and forth with opening and closing of the segment joints due to the discontinuity of the longitudinal steel bars there; after the shaking, the piers will re-center due

Correspondence to: Li Xian, Jiangsu Key Laboratory of Environmental Impact and Structural Safety in Civil Engineering, China University of Mining and Technology, Xuzhou 221116, Jiangsu, China
Tel: +86-15252008393
E-mail: lixian@cumt.edu.cn; leexian@yeah.net
[†]Professor; [‡]PhD Candidate; [§]Former Graduate Student

Supported by: National Natural Science Foundation of China under Grant Nos. 51978656 and 51478459, the Key Research and Development Project of Xuzhou under Grant No. KC22282, and the Open Fund of Jiangsu Key Laboratory of Environmental Impact and Structural Safety in Civil Engineering, China University of Mining and Technology under Grant No. KFJJ202004

Received June 23, 2021; **Accepted** January 6, 2023

to the restoring force provided by the post-tensioning tendons. The excellent self-centering behavior of traditional post-tensioned segmental piers used in regions of low seismicity have been confirmed by the studies conducted by Hewes (2002), Chou and Chen (2006), Wang *et al.* (2008), Yamashita and Sanders (2009), Tong *et al.* (2019), Xia *et al.* (2020a), Zhang *et al.* (2020a). However, these studies also pointed out that the segmental piers have much lower energy dissipation capacity than monolithic piers, and are prone to damage at the bottom-most segment due to the concrete crushing at large drift ratios. To increase the energy dissipation capacity of the piers, some researchers have proposed using energy dissipaters such as mild steel bars (Bu *et al.*, 2016; Tong *et al.*, 2019 ; Xia *et al.*, 2021; Xin *et al.*, 2022), steel angles (Elgawady and Sha'Lan, 2011) and buckling restrained dissipaters (Kam *et al.*, 2010; Marriott *et al.*, 2011; Guerrini *et al.*, 2015; Zhang *et al.*, 2020a) across the critical segment joints. To reduce the damage at the bottom-most segments, some advanced compressive performance materials such as hybrid fiber-reinforced concrete (Trono *et al*., 2015), ultrahigh-performance concrete (Ichikawa *et al*., 2016; Yang and Okumus, 2017; Wang *et al*., 2018), and engineered cementitious composites (ECC) (Billington and Yoon, 2004) were used. The confinement to the segments using fiber-reinforced polymer tubes/wraps (Elgawady and Sha′Lan, 2011; ElGawady and Dawood, 2012; Moustafa and ElGawady, 2020; Zhang *et al.*, 2020b) or steel tubes (Chou and Chen, 2006; Guerrini *et al.*, 2015; Zhang *et al.*, 2020a) was also proposed in some research. Note that the aforementioned studies mainly focused on single-column segmental concrete piers. For double-column segmental piers, more joint types such as pier-foundation joints, segment-segment joints and pier-cap beam joints exist, and the internal axial forces of double-column piers vary during a seismic event. All these result in complicated seismic responses of segmental double-column piers and need to be comprehensively studied (Zhou *et al.*, 2019; Han *et al.*, 2019; Xia *et al.*, 2020b).

Previous studies indicated that segmental concrete columns typically failed at the column footings. In this study, concrete filled steel tube (CFT) columns were employed to inhibit the crushing of column footings under cyclic loads considering the symbiotic performance of steel and concrete in CFT columns. To better understand the complicated seismic behavior of segmental double-column piers, three post-tensioned precast segmental CFT double-column pier specimens were tested under cyclic loads. The effects of the number of CFT segments and the steel endplates as energy dissipaters on the seismic behavior of the piers were evaluated. In addition, a finite element model based on OpenSEES 3.3.0 (OpenSees command manual, 2020) is introduced to efficiently simulate the seismic behavior of post-tensioned precast segmental piers. Based on the validated models, parameter analysis was conducted.

2 Experimental programs

2.1 Test specimens

To verify the seismic performance of post-tensioned precast segmental CFT double-column piers, three specimens labelled as DC-PSC1–DC-PSC3 were tested under simulated seismic loads, as shown in Fig. 1 and Table 1. Each specimen consisted of one reinforced concrete foundation, two CFT columns and one cap beam. The clear span of the double CFT columns was 1000 mm, while the clear height of the two columns was 1200 mm. The circular steel tubes for the CFT columns had an outer diameter of 219 mm and a wall thickness of 6 mm. The cap beam was a concrete filled U-shaped steel beam and the dimensions of the beam were 2000 mm (length) × 550 mm (width) × 450 mm (depth). The U-shaped steel was rolled by a 4 mm-thick steel, and its upper opening was connected by nine steel plates (430 mm × 50 mm × 5 mm) with a spacing of 250 mm. The reinforced concrete foundation had the dimensions of 2200 mm (length) × 750 mm (width) × 600 mm (depth), and were heavily reinforced using Φ18 flexural reinforcement and Φ8 stirrups to remain almost elastic during the test.

The CFT columns, cap beams and foundations were precast independently in the laboratory and a 50 mm-diameter duct was set at the center of the column′s cross section for passing through high-strength bars. In these tests, each CFT column was connected to the foundation and the cap beam using one un-bond 32 mm-diameter high-strength bar, which was posttensioned to 390 before the test according to the study conducted by Chou and Chen (2006). The corresponding tensile stress of posttensioning (PT) bar was 486 MPa, accounting for 45% of its yield strength (1080 MPa), which ensures that it remains in an elastic state during the entire test process.

Among these three specimens, the only differences were in the details of the CFT columns. Each column in specimen DC-PSC1 was constructed by using one

Table 1 Details of tested specimens

Specimen No.	CFT columns	The number of segments	Energy dissipaters
DC-PSC1	Φ219×6 tube 40.6 MPa infilled concrete	1	No
DC-PSC2		3	No
DC-PSC23		3	Bolted steel endplates with a thickness of 10 mm

monolithic 1200 mm high CFT segment, while each column in specimens DC-PSC2 and DC-PSC3 was constructed by using three 400 mm-high CFT segments. In specimen DC-PSC3, the two ends of each column were welded with square steel endplates (420 mm × 420 mm × 10 mm) as external energy dissipaters. The endplates were connected to the cap beam and foundation by four embedded Grade 8.8 bolts with a diameter of 12 mm.

2.2 Material properties

The compressive strength of the concrete was obtained by compression tests of 150 mm concrete cubes at the time of specimen testing as per the Chinese standard for test method of mechanical properties on ordinary concrete. The concrete for reinforced concrete foundations had a measured compressive strength of 45.8 MPa, while the CFT columns and cap beams were filled using concrete with compressive strength of 40.6 MPa. The yield strength and the tensile strength of each steel component was obtained by testing three tensile coupons, as shown in Table 2. The 32 mm-diameter high strength bars had the yield strength and the ultimate strength of 1080 MPa and 1230 MPa, respectively, as provided by the manufacturer.

2.3 Test methods

Figure 2 shows the test setup for all specimens. The concrete foundation of the specimen was first fixed to the strong floor using eight steel rods, and then the vertical axial load from the superstructures was loaded at the mid-span of the cap beam using a steel lever beam post-tensioned by two rocking high-strength steel rods. The total axial load kept constant to 700 kN during the whole tests and the axial compression ratio was about 0.1 for each column. The lateral cyclic load was applied to the cap beam at a height of 1360 mm above the top of the foundation, and the loading sequence was controlled by the drift ratio. Herein the drift ratio was defined as the

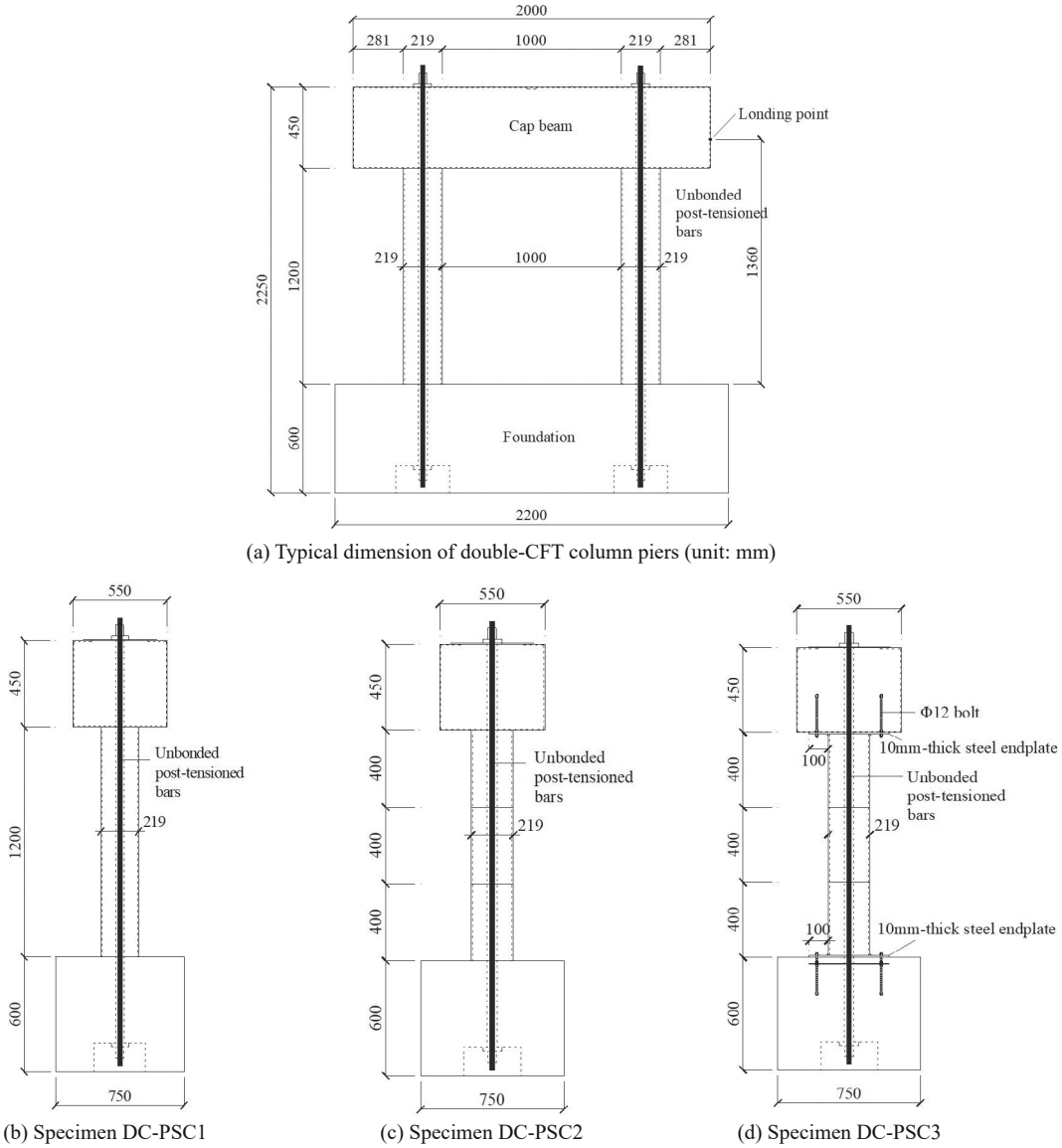

(a) Typical dimension of double-CFT column piers (unit: mm)

(b) Specimen DC-PSC1 (c) Specimen DC-PSC2 (d) Specimen DC-PSC3

Fig. 1 Details of tested specimens

Table 2 Properties of steel and rebar

Type	Yield strength (MPa)	Ultimate strength (MPa)
Rebar Φ8	376	501
Rebar Φ18	400	578
Steel plate of cap beam (4 mm)	274	427
Steel tube (6 mm)	376	538

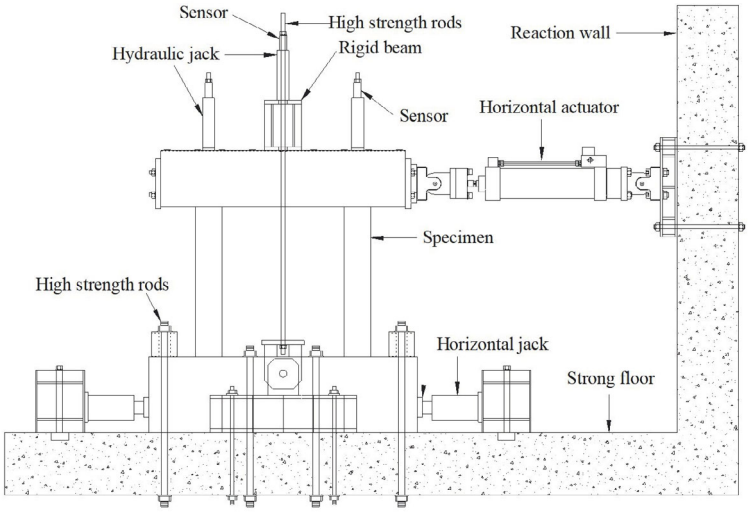

Fig. 2 Test setup

applied horizontal displacement relative to the loading height of 1360 mm. The drift ratios θ including ±0.25%, ±0.5%, ±0.75%, ±1%, ±1.5%, ±2%, ±3%, ±4%, ±5%, ±6%, ±7%, ±8%, ±9%, ±10%, ±11%, ±12% and ±13% were applied. The tests stopped at the drift ratio of 13% since it was too dangerous to further increase it. During the testing, the drift ratios smaller than 1.0% were loaded with one cycle for each. For the drift ratio θ =1.0%–4.0%, three cycles for each were carried out to evaluate the strength and stiffness degradation of the specimens. After the drift ratio of 4%, the loading cycles were repeated twice.

During the tests, the applied lateral loads, the axial load and the post-tensioned forces of the CFT columns were monitored using calibrated load cells, while the lateral deformations and the joint opening of column ends were monitored by separate linear potentiometers. The circumferential and vertical strains of CFT columns were also measured by electrical resistance strain gauges.

3 Experimental results and discussion

3.1 General performance and hysteretic behavior

Figure 3 presents the damage modes of all three tested specimens at the drift ratio of 13%. The hysteretic curves of the specimens are shown in Fig. 4 with the measured lateral force, P, versus the loading displacement, Δ, as well as the drift ratio, θ. The skeleton curves for the lateral force versus the lateral drift ratio are also included in Fig. 4, which was obtained using the peak points of the first cycle of each load level.

As shown in Figs. 3 and 4, the damage modes and the hysteretic behavior of post-tensioned precast segmental CFT double-column piers were quite different from those of monolithic CFT columns with fixed column bases. In these tests, the joint opening at the column ends released the tensile stress of the steel tubes, avoiding the tensile fracture of the steel tubes that usually occurred during cyclic lateral testing of monolithic CFT columns. As evidenced by Fig. 3, the steel tubes suffered from symmetrical buckling at the column ends due to the bearing of the segments against the foundation and the cap beam. However, due to the good confinement provided by the steel tubes, the concrete cores were not crushed and the loading capacities of all three specimens deteriorated very slowly with the increase of the loading amplitudes and loading cycles. As shown in Fig. 4, the rocking of CFT column ends also resulted in much narrower hysteresis loops and smaller residual displacements. The detailed damage processes of the tested specimens are described as follows.

(1) Specimen DC-PSC1

Specimen DC-PSC1 exhibited nearly linear elastic performance until a drift ratio of 1.5%. The visible opening of the beam-column and the column-foundation interface joints started at the drift ratio of about 2%, resulting in a column rocking mechanism. The maximum joint opening at the two ends of each

CFT column reached about 5 mm at the drift ratio of 3%. After that, the loading capacity of the specimen remained almost constant as the applied displacements increased. At the drift ratio of 5%, the joint openings increased to 10 mm and slight buckling of the CFT columns′ top ends was also observed, as evidenced by the falling of the whitewash painting on the CFT columns. The local crushing of the concrete cover of the foundations around the CFT columns started at the drift ratio of 6% due to too large local compression induced by the columns. The maximum joint opening of the column ends reached 20 mm at the drift ratio of 9% and 25 mm at the drift ratio of 12%. The testing of specimen DC-PSC1 stopped at the first cycle of 13% drift ratio due to the too large drift ratio. At the drift ratio of 13%, the symmetrical buckling of the column ends became very serious under cyclic local compression and the concrete cover of the foundation was seriously crushed around the CFT columns; however, the average loading drop of the specimen was about only 9% due to the good confinement of column ends provided by the ductile steel tubes. The specimen experienced its average peak loading capacity of 246 kN during the test.

(2) Specimen DC-PSC2

The damage process of specimen DC-PSC2 was similar to that of specimen DC-PSC1. There was no visible damage prior to the drift ratio of 2%. The maximum joint opening of column ends reached 5 mm at the drift ratio of 3%, 8 mm at the drift ratio of 5%, 15 mm at the drift ratio of 7%, 20 mm at the drift ratio of 9% and 25 mm at the drift ratio of 12%. The symmetrical buckling of the top ends of the CFT columns started at the drift ratio of 5% and the extent of the buckling developed as the applied drift ratios increased. When the drift ratios reached 13%, the rocking of the CFT column ends was obvious, and the local concrete crushing of the foundation around the column bottom ends was serious. However, no significant drop of the loading capacity of the specimen DC-PSC2 was found even at this large drift. During the whole test, the joint opening only occurred at the column ends, and no obvious slipping at the segment-to-segment interfaces was found. The specimen achieved a maximum loading capacity of 238 kN, which was comparable to that of specimen DC-PSC1. This result indicated that the number of CFT segments had no significant effects on the loading capacity. This is because the CFT columns had desirable compressive behavior and no visible joint opening between segments occurred under the compression of both axial loads and post-tensioned forces.

(3) Specimen DC-PSC3

For specimen DC-PSC3, steel endplates as external energy dissipaters were welded to the top and bottom ends of the CFT columns, and were bolted to the cap beam and the foundation. The steel endplates effectively inhibited the joint opening at the column ends at the small drift ratios and no visible damage of the specimen occurred until the drift ratio of 4%. The buckling of the endplates under bending was observed at the drift ratio of 4% and the CFT columns buckled at the drift ratio of 5%. The buckling of the steel endplates and the columns developed as the drift ratios increased. One bolt

(a) Specimen DC-PSC1

(b) Specimen DC-PSC2

(c) Specimen DC-PSC3

Fig. 3 Damage to tested specimens at the final conditions

for endplates was fractured at the drift ratio of 9% and then the remaining bolts were progressively fractured as the applied displacement increased. Since the bolted steel endplates were designed when the energy dissipation devices and the endplates were thin, the fracture of the bolts did not result in an obvious drop of the loading capacity of the specimen. The test continued due to the good work of the post-tensioned bars until the first cycle of the drift ratio reached 13% for safety considerations. During this test, the concrete cover of the foundation was not crushed since the endplates expanded the compression zones at the column ends. The use of endplates in specimen DC-PSC3 resulted in fatter hysteretic loops and higher loading capacity. This specimen got a maximum loading capacity of 329 kN, which was 38.2% higher than that of specimen DC-PSC2.

3.2 Stiffness and stiffness degradation

The stiffness characteristics of the tested specimens were evaluated using peak-to-peak stiffness, which was obtained by dividing the peak load at the first cycle of each deformation level by its corresponding displacement. As shown in Fig. 5(a), specimen DC-PSC1 with a 1200 mm high CFT segment for each column exhibited the highest initial stiffness of 22.9 kN/mm. Though no visible joint opening between segments was found during the test, the initial stiffness of the specimen reduced due to the increase of the number of segments. Specimen DC-PSC2 with three segments for each column had the initial stiffness of 19.4 kN/mm, which was about 84.7% that of specimen DC-PSC1. However, with the increase of the applied drift ratios, the difference of the stiffness between the two specimens was reduced, and the two specimens had nearly the same stiffness beyond the drift ratio of 1.5%. The use of steel endplates increased the initial stiffness of the specimen and reduced the deterioration rate of the stiffness. Though specimens DC-PSC2 and DC-PSC3 had the same number of segments for each column, the initial stiffness of specimen DC-PSC3 was 9.3% higher than that of specimen DC-PSC2. It can also be found that the stiffness of specimen DC-PSC3 was higher than those of the other two specimens when the drift ratios were larger than 0.75%.

The stiffness degradation rates of the tested specimens were evaluated using the peak-to-peak stiffness normalized by their corresponding initial stiffness, as shown in Fig. 5(b). The normalized peak-to-peak stiffness k/k_t was also fitted using Eq. (1).

$$\frac{k}{k_t} = 0.68\theta^{-0.85} \le 1 \tag{1}$$

where θ is the drift ratio (%).

As shown in Fig. 5(b), the stiffness of the tested

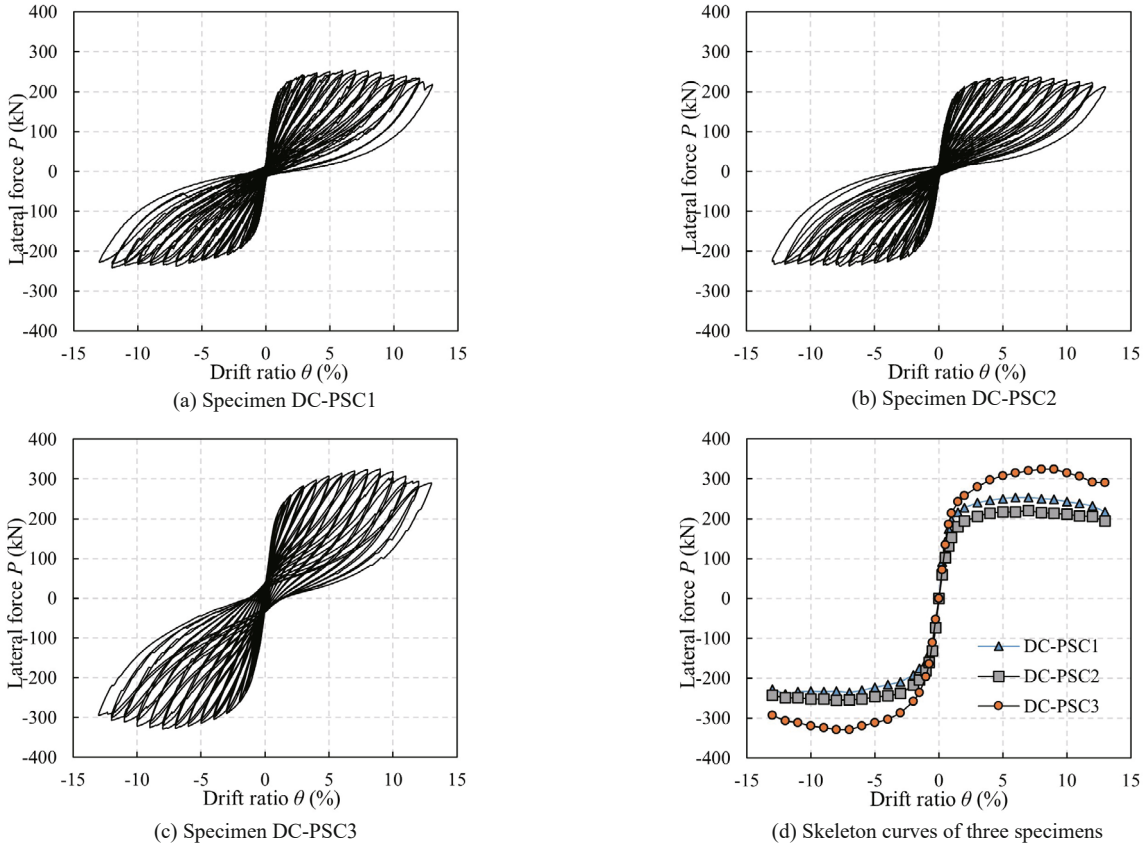

(a) Specimen DC-PSC1 (b) Specimen DC-PSC2

(c) Specimen DC-PSC3 (d) Skeleton curves of three specimens

Fig. 4 Hysteresis curves and skeleton curves of tested specimens

specimens deteriorated as the applied displacement increased. The stiffness degradation was mainly attributed to the opening of column-foundation and column-cap beam joints and the buckling of CFT segments. Specimen DC-PSC1 had the most rapid stiffness degradation. The use of a steel endplate resulted in much slower stiffness degradation of specimen DC-PSC3. From a comparison of the test and predicted normalized stiffness, it can be seen that Eq. (1) well predicts the stiffness degradation of segmental columns.

3.3 Energy dissipation capacity

The energy dissipation capacity and the residual displacement after strong earthquakes are two important performance indices to evaluate the seismic behavior and self-centering ability of posttensioned segmental piers. According to the study conducted by Ou *et al.* (2007) and Cai *et al.* (2018), the increase of the energy dissipation capacity of piers usually results in the reduction of their self-centering ability. Herein the energy dissipation capacity of the tested specimens was evaluated by both the energy dissipation coefficient E_h and the cumulative energy dissipation, as shown in Fig. 6. The detailed definition of both the energy dissipation coefficient E_h and the cumulative dissipated energy can be found in Li *et al.* (2015). The coefficient E_h is defined as the ratio between the strain energy measured at the peak deformation and the total energy dissipation at each cycle. The cumulative energy dissipation is calculated using the area enclosed by the load-deformation hysteresis loop.

As shown in Fig. 6(a), the energy dissipation coefficient versus drift ratio curves of post-tensioned segmental piers without energy dissipaters were different from the CFT double-column/pile frames with rigid connections tested by Li *et al*. (2020), of which the energy dissipation coefficients increased with increase of the applied displacements due to the formation of plastic hinges. The energy dissipation coefficients of specimens DC-PSC1 and DC-PSC2 were similar and varied around 0.35, indicating that the number of segments has little effect on the energy dissipation. Due to the damage in the steel tubes and concrete cores, the coefficients of these two specimens reduced gradually after the drift ratios of 3%. For specimen DC-PSC3, the plastic deformation of the steel endplates significantly enhanced the energy dissipation coefficient at the large drift ratios. The energy dissipation coefficient of specimen DC-PSC3 reached a maximum value of 0.52 at the drift ratio of 9%, where

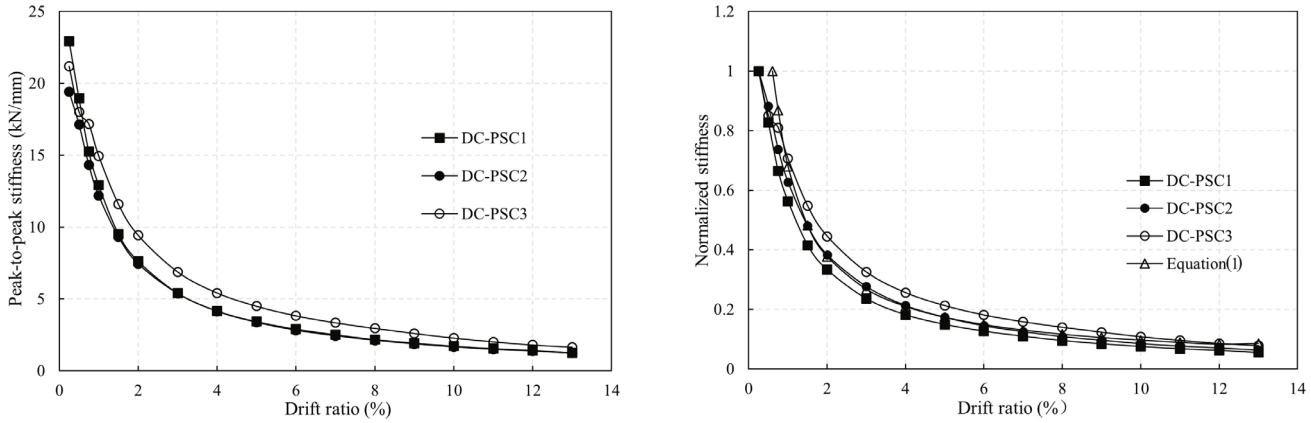

(a) Peak-to-peak stiffness (b) Normalized peak-to-peak stiffness

Fig. 5 Stiffness of the tested specimens

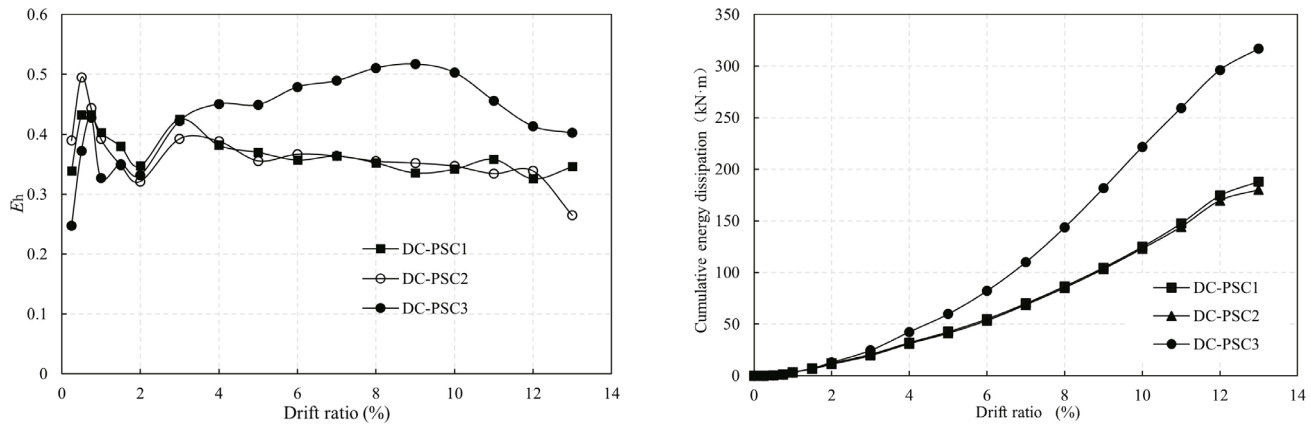

(a) Energy dissipation coefficient curves (b) Cumulative energy dissipation

Fig. 6 Energy dissipation capacity of tested specimens

the bolts for the steel endplates started to be fractured.

The cumulative energy dissipation versus the drift ratio curves of all tested specimens are presented in Fig. 6(b). It can be seen that specimens DC-PSC1 and DC-PSC2 had the cumulative energy dissipation curves which were substantially coincidental. This is because the joint opening of these two specimens concentrated on the column ends and the energy dissipation was mainly induced by the plastic compression deformation of the CFT column ends. At the drift ratio of 13%, the cumulative energy dissipation of DC-PSC1 and DC-PSC2 was 188 kN·m and 180 kN·m, respectively. The plastic deformation of steel endplates significantly increased the cumulative energy dissipation of specimen DC-PSC3 to 316 kN·m at the drift ratio of 13%, which was 75.5% higher than that of specimen DC-PSC2.

3.4 Residual displacement

The residual displacement is defined as the lateral displacement at the pier top, when the imposed lateral force is unloaded to zero at each loading cycle, as shown in Fig. 7. The residual displacement ratio was obtained by dividing the residual displacement by the loading height. A specimen with a small residual displacement after unloading shows good self-centering capacity and a pier with residual displacement ratios smaller than 1% usually can be repaired after a strong earthquake. Figure 7 plots the average residual displacement at each drift ratio. It can be seen that the residual displacements increased linearly as the applied displacements increased when the drift ratios were lower than 10%. Specimens DC-PSC1, DC-PSC2 and DC-PSC3 had residual displacement smaller than 1% until 11%, 12% and 8% drift ratios, respectively, showing a good self-centering capacity. The increase of the segment numbers resulted in larger residual displacement of specimen DC-PSC2 at the drift ratios lower than 3%. However, the residual displacements of specimen DC-PSC1 increased relatively rapidly and exceeded those of DC-PSC2 beyond 3% drift ratios. Specimens DC-PSC2 and DC-PSC3 had comparable residual displacements at drift ratios smaller than 3%. After that, the residual displacement of specimen DC-PSC3 increased rapidly due to the plastic deformation of steel endplates. At the drift ratio of 10%, the residual displacement of specimen DC-PSC3 was 2.11 times that of specimen DC-PSC2. It can also be found that due to the fracture of anchor bolts, the residual displacements of the specimens decreased after the drift ratio of 10%.

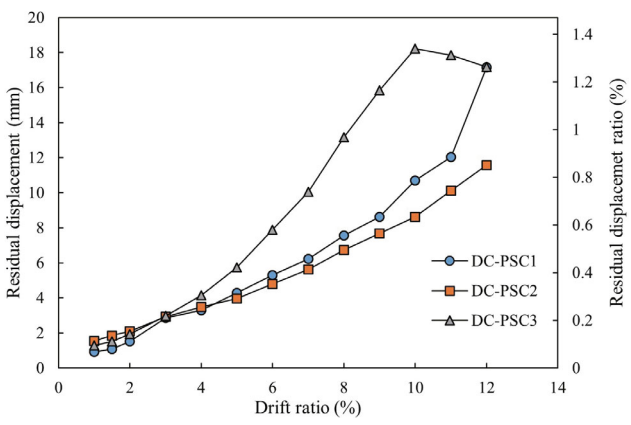

Fig. 7 Residual displacements of the specimens

3.5 Column rotation

The joint opening of the tested specimens was concentrated in the column-foundation joints and the column-cap beam joints and the rotations of these joints were monitored during the tests. The rotation angle θ_c is defined as

$$\theta_c = \frac{\Delta_t - \Delta_c}{b_t} \tag{2}$$

where Δ_t is the elongation of a displacement transducer on the tension side of the joints; Δ_c is the shortening of a displacement transducer on the compression side of the joints, and b_t is the displacement between those two displacement transducers. Note that the displacement transducers for Δ_t and Δ_c were fixed on the CFT columns at the height of 200 mm to the top surfaces of the foundations or the bottom surfaces of the cap beams. Thus, Δ_t and Δ_c were composed of the joint opening values at column ends and the elastic and plastic deformations of the columns themselves at these regions.

Typical lateral force versus column rotation curves are presented in Fig. 8. It can be seen that three tested specimens had comparable column rotation at the column-to-cap beam joint and the column-to-foundation joint. Specimen DC-PSC1 with one segment for each column had the largest rotation at the column ends and the largest residual rotation after unloading. This result indicated that the columns of specimen DC-PSC1 suffered more serious local buckling at the column ends. The column rotation reached about 0.15 at the drift ratio of 13%. The increase of the number of segments in specimen DC-PSC2 resulted in relatively small rotation at the column ends and the specimen had the rotation of about 0.12 at the drift ratio of 13%. The use of steel endplates as energy dissipaters increased the residual rotation of column ends due to the relatively significant plastic deformation of the CFT column ends.

3.6 Posttensioning forces

For each specimen, two calibrated load cells were used to monitor the forces of the PT bars in two columns named as column A and column B, under a constant vertical load and cyclic lateral loads. Figure 9 shows the variation of the posttensioning forces of the tested

specimens. It can be seen that as the lateral displacement increased, the posttensioning force of the PT bars increased significantly since the joint opening, as a result of the rocking mechanism, caused additional elongation of the PT bars. Fortunately, the force developed in the PT bar was well below its yield force of 868 kN until the drift ratio of 13%. The average maximum posttensioning forces of PT bars in specimens DC-PSC1, DC-PSC2 and DC-PSC3 were 575kN, 582 kN and 657 kN, respectively, which were 48%, 49% and 66% higher than the initial posttensioning force, respectively. This result indicated that the number of segments had no significant effect on the response of the posttensioning forces; however, the use of steel endplates increased the bending moment at the column ends and increased the posttensioning forces of PT bars. Since the axial forces of the double-column piers varied during the cyclic tests, the amount of the change of the posttensioning forces was asymmetric under positive and negative loads, and the PT bars for the column at the potential tension side had a large amount of the change of the posttensioning forces.

From the figure, it can also be seen that the cyclic lateral loads resulted in the loss of posttensioning forces of PT bars due to the axial deformation of the CFT columns. For example, the posttensioning force of PT bars in column A of specimen DC-PSC1 ranged from 49 kN to 553 kN during the drift ratio of 12%. The posttension loss reached 87.4% of initial posttensioning force. However, the loss of posttensioning forces of PT bars did not result in significant deterioration of the self-centering capacity of the specimens. Note that the posttension loss ratios were similar to that of PT bars for

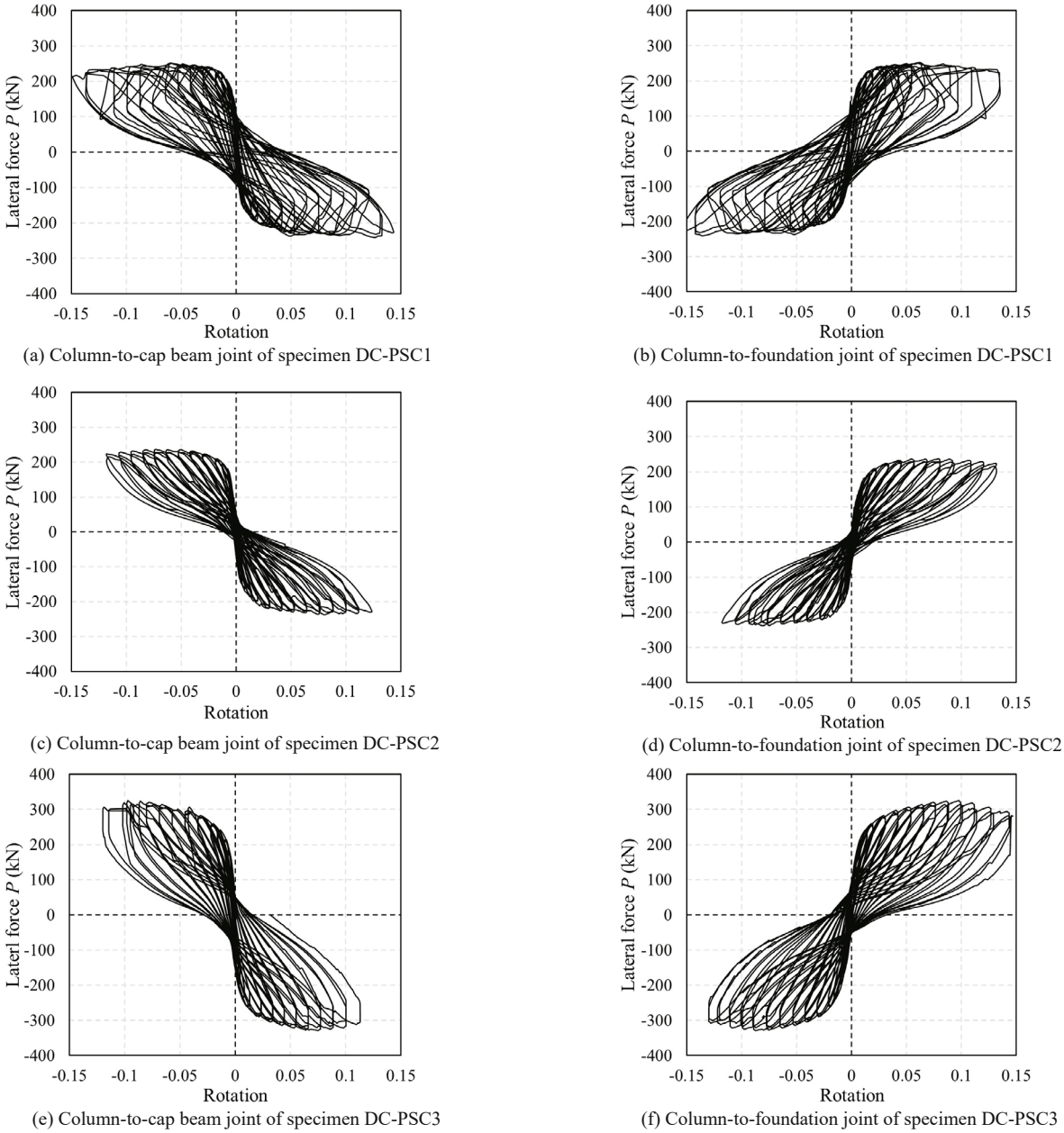

(a) Column-to-cap beam joint of specimen DC-PSC1

(b) Column-to-foundation joint of specimen DC-PSC1

(c) Column-to-cap beam joint of specimen DC-PSC2

(d) Column-to-foundation joint of specimen DC-PSC2

(e) Column-to-cap beam joint of specimen DC-PSC3

(f) Column-to-foundation joint of specimen DC-PSC3

Fig. 8 Typical column rotation of tested specimens

double fiber tube confined concrete column piers tested by ElGawady *et al.* and Sha′Lan (2011) but much larger than those of PT bars for double-reinforced concrete column piers tested by Han *et al.* (2019). The test conducted by Yang and Okumus (2017) also indicated the segmental columns constructed using ultrahigh-performance concrete had large posttension loss due to the concentrated damage and joint opening at the column-foundation joints and the column-cap beam joints.

4 Numerical modeling and parameter analysis

4.1 Numerical models and model validation

Based on the nonlinear structural analysis program OpenSEES 3.3.0 (OpenSees command manual, 2020), the method of simulating the seismic behavior of posttensioned precast segmental CFT double-column piers DC-PSC2 using a fiber model was developed, as shown in Fig. 10. The CFT column segments were

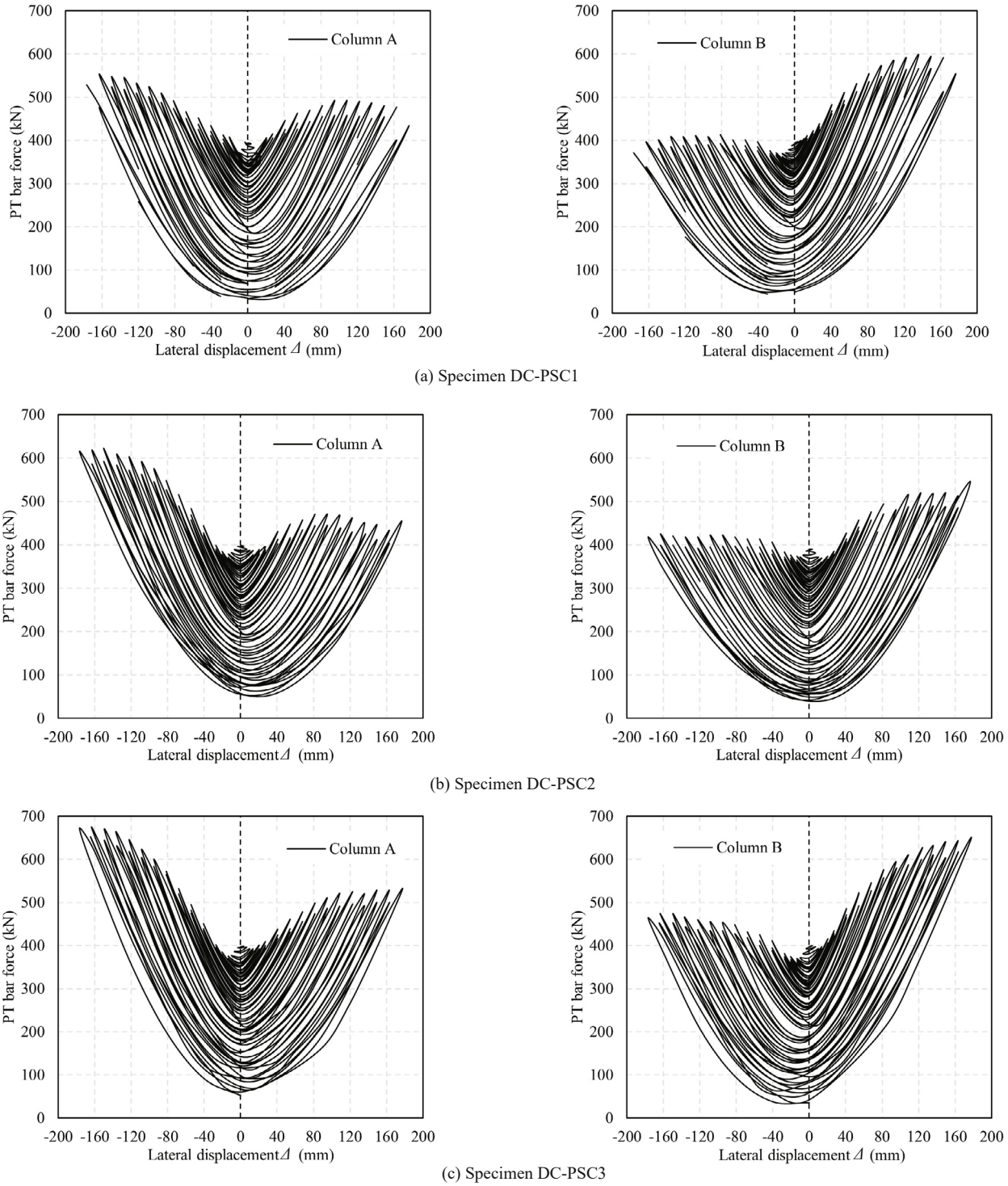

(a) Specimen DC-PSC1

(b) Specimen DC-PSC2

(c) Specimen DC-PSC3

Fig. 9 Variation of the PT forces

modeled using the DispBeamColumn element, where each section was composed with steel tube fiber and core concrete fiber. The core concrete was modeled using the Concrete02 material model and the stress-strain curve was determined by the modified Kent-Park model (Scott *et al*., 1982) with consideration of the confinement effects. The steel tubes of CFT columns were modeled using the Steel02 material model with a post-yield tangent modulus of 0.001 times the elastic modulus. The interface joints between segments were modeled using the zeroLengthSection element, where each section was also composed with concrete fiber and steel tube fiber but with different material models. Since significant plastic deformation of both the steel tube and the confined concrete core were observed at the column ends, both the core concrete and the steel tubes at the interface joints were modeled using the ElasticPPGap material model with only compression strength. Therefore, the joints can open at the tension side. The unbonded PT bars were modeled with corotTruss elements with two ends connected by the cap beam and the bottom of the foundation, respectively. The initial posttension force of the bars was modeled using the Steel02 material model with initial strain. The concrete filled U-shaped steel cap beam was modeled using elasticBeamColumn elements.

Based on the DC-PSC2 model, specimen DC-PSC1 was modeled by removing all joint elements between segments. The DC-PSC3 model was also developed based on the model DC-PSC2 considering that the bolted steel endplate reduced the joint opening. The ElasticPPGap material of the zeroLengthSection element for the column-footing or cap beam joint was paralleled with steel02 material to model the effects of a bolted endplate. The equivalent steel02 material had the equivalent yield strength determined by the yield strength of the bolts considering that the bolt fracture occurred during the test, and the tensile stiffness was calculated by assuming the endplate as a beam fixed by the bolts.

As show in Figs. 11 and 12, the hysteretic curves and the posttensioning force response curves predicted by the developed fiber model were well within the experimental results, indicating that the analytical model can reasonably predict the hysteretic behavior of segmental piers and can be used for parametric analysis. Since the hysteretic responses of columns A and B in the specimens were difficult to monitor during the tests,

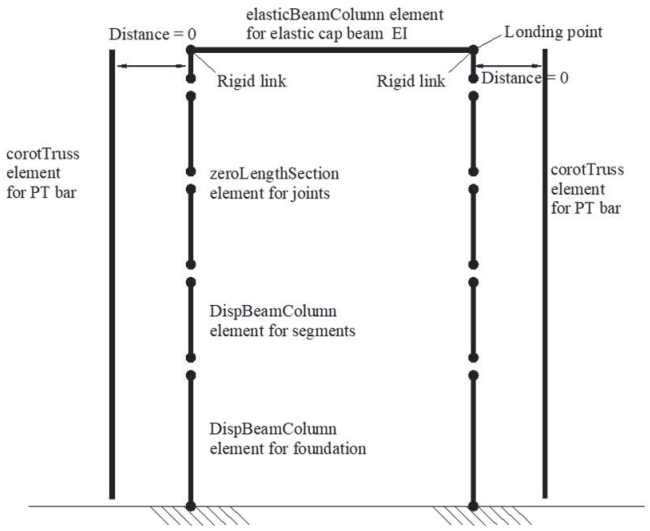

(a) Fiber element model

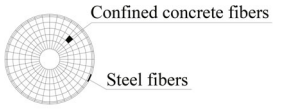

(b) Fiber section for segments and Zero-length joints

Fig. 10 Analytical model of the specimens using OpenSees

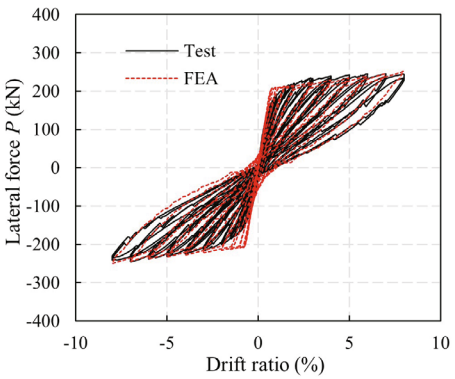

(a) Specimen DC-PSC1

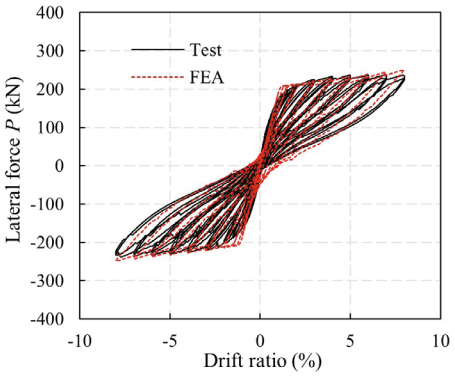

(b) Specimen DC-PSC2

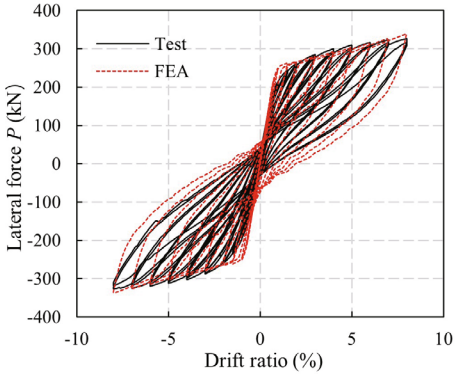

(c) Specimen DC-PSC3

Fig. 11 Comparisons of experimental and FEA hysteretic curves

the numerical results are presented in Fig. 13. Due to the asymmetrical responses of the PT bars under cyclic loading, the hysteretic responses of columns A and B were asymmetrical. For specimen DC-PSC2, the difference at the positive and negative directions was 19 kN at the drift ratio of 8%.

4.2 Effects of segment numbers

Based on the model DC-PC2 without energy dissipaters, the effects of the segment numbers were studied by assuming each CFT column with the same total column height but different segment numbers. As shown in Fig. 14, as the segment numbers increased from 2 to 4, the changes of the strength, deformation capacity and energy dissipation capacity of the segmental piers were not obvious; however, the initial stiffness of the specimens was reduced. These results can be explained as follows: the PT bar effectively restrained the joint opening between segments, and thus the joint opening and plastic deformation were mainly concentrated at the column ends even at large column lateral drifts. The good confinement provided by the steel tube successfully avoided the concrete crushing at the column ends.

4.3 Effects of the axial loads and prestress levels

The effects of two types of loading conditions on

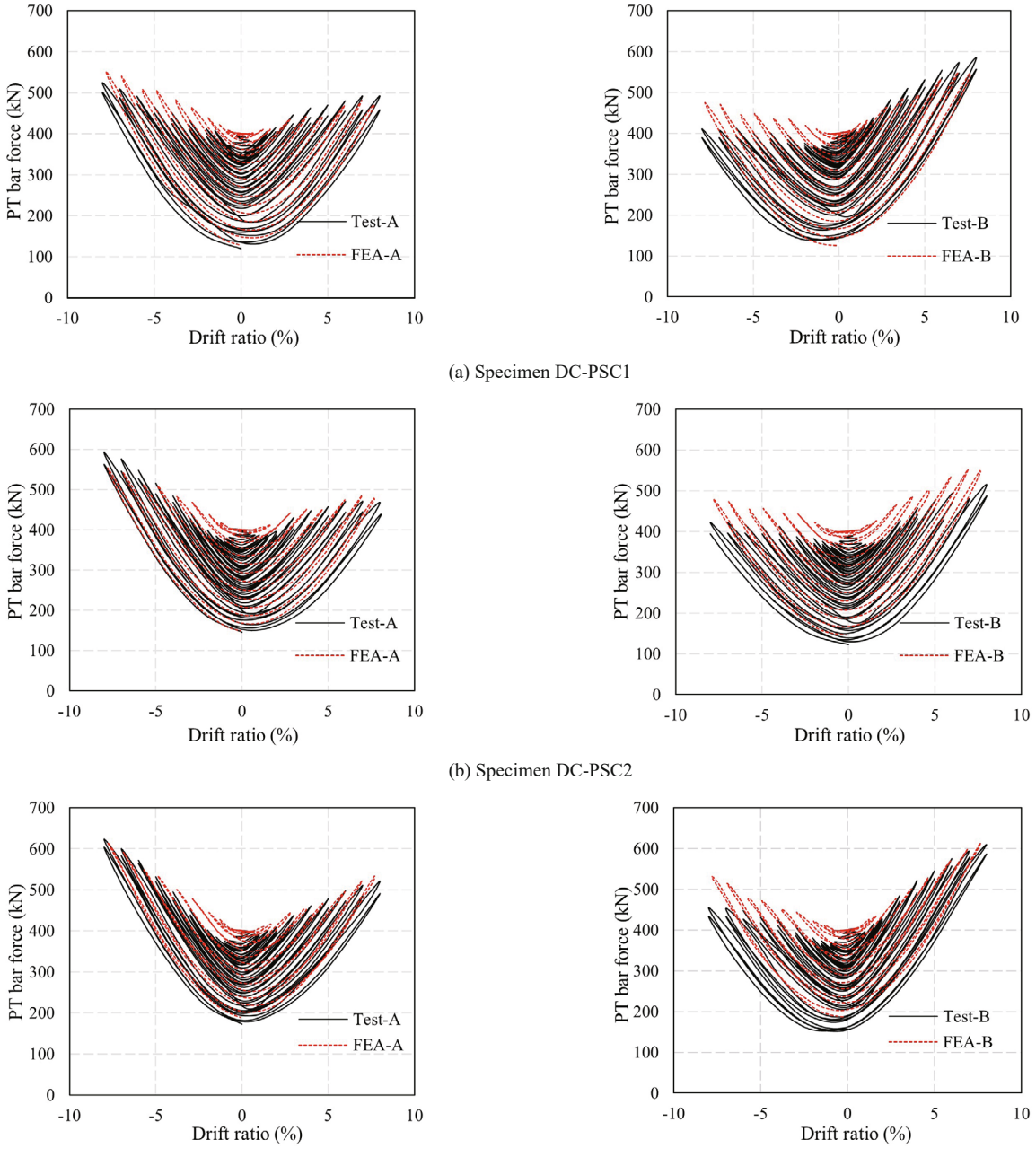

(a) Specimen DC-PSC1

(b) Specimen DC-PSC2

(c) Specimen DC-PSC3

Fig. 12 Comparisons of experimental and FEA PT forces curves

the seismic behavior of the double-column piers were studied based on the DC-PSC2 fiber model. One was to keep the axial force constant while changing the prestress of the PT bars. The other was to change both the axial force and the prestress but the sum of the two loads was constant. The hysteretic curves and skeleton curves of the specimens are shown in Figs. 15 and 16, respectively. In these figures, the load combination means "axial load + prestress of PT bars". The comparison of the results of specimens under the load combination of "350+400" and "450+300" indicate that the axial loads and the prestress of the PT bars had similar effects on the seismic behavior of the specimens since the hysteretic curves of these two specimens were essentially the same.

From Fig. 16, it can be seen that the change of the axial loads and the prestress had little effect on the initial stiffness of the specimens if their sum was constant. However, under the constant axial force, the strength and the energy dissipation of the specimens increased as the prestress of PT bars increased. At the drift ratio of 8%, the strength of the specimens under the load combinations of "350+200" , "350+300", "350+400", "350+500" and "350+600" were about 225 kN, 237 kN, 250 kN, 262 kN and 275 kN, respectively. In other words, the strength increased by about 5% with 25% increase of the prestress, which indicated that the prestress had some impact on the strength but the increase amount of the strength was relatively small when compared with that of the prestress.

The cumulative energy dissipation versus the drift ratio curves are presented in Fig. 17. It can be seen that all the specimens exhibited similar energy dissipation capacity before 1.5%; however, the effects of the prestress gradually became obvious as the applied drift ratio increased. At the drift ratio of 8%, the cumulative energy dissipation capacities of the specimens under the load combinations of "350+200", "350+300", "350+400", "350+500" and "350+600" were about 46 kN·m, 54 kN·m, 61 kN·m, 68 kN·m and 75 kN·m, respectively. In other words, the cumulative energy dissipation capacity increased by about 11% with about 25% increase of the prestress, indicating that the prestress had an obvious

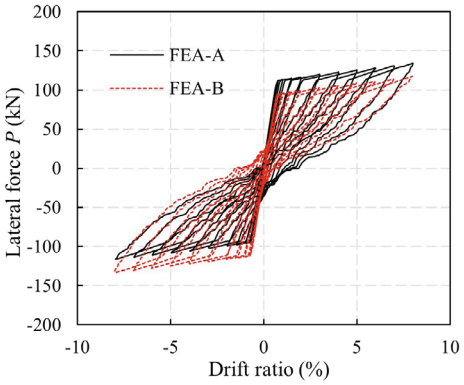

(a) Specimen DC-PSC1

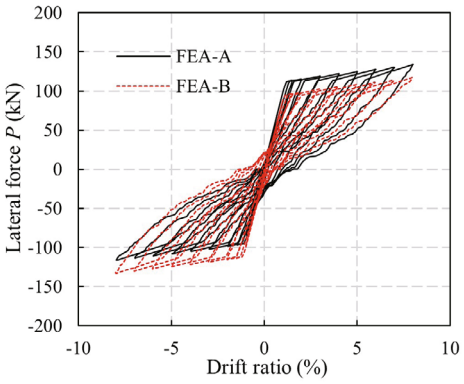

(b) Specimen DC-PSC2

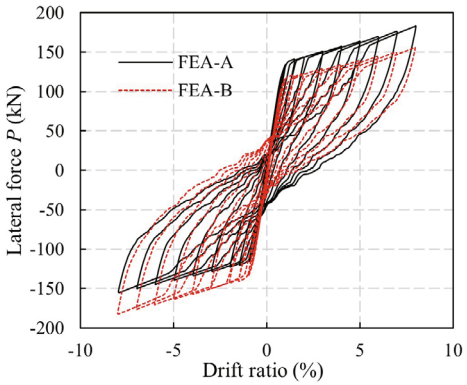

(c) Specimen DC-PSC3

Fig. 13 Hysteresis curves of each single column

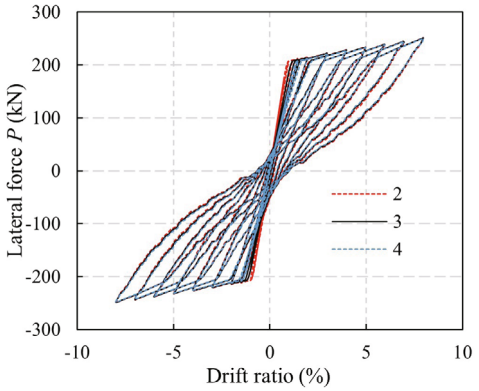

Fig. 14 Hysteretic curves of specimens with different segment numbers

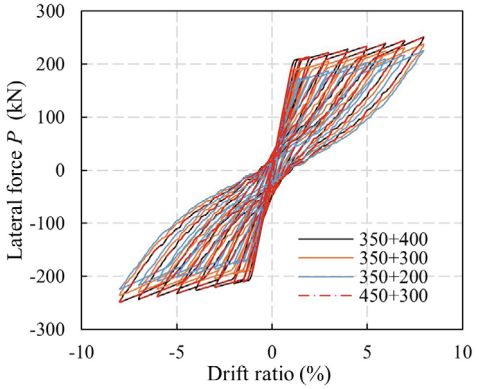

Fig. 15 Hysteretic curves of specimens under different load states

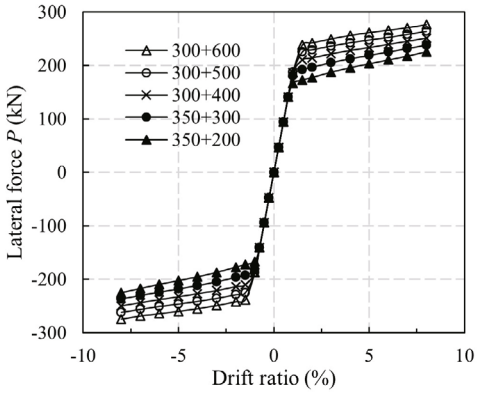

Fig. 16 Skeleton curves of specimens under different load states

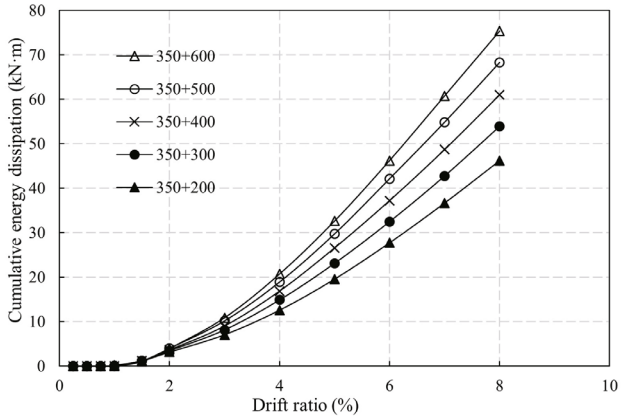

Fig. 17 Cumulative energy dissipation of specimens under different load states

effect on the cumulative energy dissipation capacity of the specimen. The increase of the energy dissipation was mainly attributed to the increase of the plastic deformation of the joints at the column ends.

5 Conclusions

Experimental and numerical studies on the seismic behavior of post-tensioned precast segmental CFT double-column piers were carried out in this study, and the following conclusions can be drawn:

(1) The post-tensioned precast segmental CFT double-column piers exhibited stable hysteretic behavior with small residual displacements under strong earthquakes. All the tested specimens achieved a drift ratio no less than 13% without significant damage and strength deterioration due to the desirable performance of the CFT columns. Damage to the specimens was quite different from that of the conventional CFT column embedded into the foundation. The damage was concentrated in the local buckling of the steel tubes due to the bearing of the segments against the foundation and cap beam. No concrete crushing at the column ends occurred during the test.

(2) The experimental and analytical results indicated that for the specimens without additional energy dissipaters, the effects of segment numbers on the strength, deformation capacity and energy dissipation of segmental piers were not obvious since both the joint opening and the plastic deformation were primarily concentrated at the column ends. However, the increase of segment numbers had an adverse effect on the initial stiffness of the specimen. It can also be found that the specimen with one monolithic segment for each column had more serious local buckling at the column ends, resulting in larger rotations at the column ends and larger residual displacements.

(3) The use of steel endplates as energy dissipaters improved the bearing capacity, stiffness and energy dissipation of the segmental piers. Compared with the test results of specimen DC-PSC2, the bearing capacity, elastic stiffness and cumulative energy dissipation of specimen DC-PSC3 with steel endplates were increased by 28.5%, 3.8%% and 68%, respectively. However, the steel endplates seriously weakened the self-centering capacity of the specimen. Specimen DC-PSC3 had a residual displacement of 2.11 times that of specimen DC-PSC2 at the drift ratio of 10%.

(4) The posttensioning forces of the PT bars in segmental double-column piers varied significantly during the tests. However, the variation of the posttensioning forces did not result in significant deterioration of the self-centering capacity and the loading capacity of the specimens.

(5) The proposed analytical models based on fiber models can well predict the hysteretic behavior of the post-tensioned precast segmental CFT double-column piers. The analytical results indicate that the increase of the prestress of PT bars increased the strength and the energy dissipation capacity of the specimens under constant axial force. The axial loads and the prestress of the PT bars had similar effects on the seismic behavior of the specimens.

Acknowledgment

This research was funded by the National Natural Science Foundation of China (51978656 and 51478459) and the Key Research and Development Project of Xuzhou (KC22282). The experiments were also partially funded by the open fund of Jiangsu Key Laboratory of Environmental Impact and Structural Safety in Civil Engineering, China University of Mining and Technology (KFJJ202004).

References

Billington SL, Barnes RW and Breen JE (1999), "A Precast Segmental Substructure System for Standard Bridges," *PCI Journal*, **44**(4): 56–73.

Billington SL and Yoon JK (2004), "Cyclic Response of Unbonded Posttensioned Precast Columns with

Ductile Fiber-Reinforced Concrete," *Journal of Bridge Engineering ASCE*, **9**(4): 353–363.

Bu Z, Guo J, Zheng R, *et al*. (2016), "Cyclic Performance and Simplified Pushover Analyses of Precast Segmental Concrete Bridge Columns with Circular Section," *Earthquake Engineering and Engineering Vibration*, **15**(2): 297–312.

Cai ZK, Wang ZY and Yang TY (2018), "Experimental Testing and Modeling of Precast Segmental Bridge Columns with Hybrid Normal- and High-Strength Steel Rebars," *Construction and Building Materials*, **166**(2018): 945–955.

Chou CC and Chen YC (2006), "Cyclic Tests of Post-Tensioned Precast CFT Segmental Bridge Columns with Unbonded Strands," *Earthquake Engineering and Structural Dynamics*, **35**: 159–175.

Elgawady MA and Sha′Lan A (2011), "Seismic Behavior of Self-Centering Precast Segmental Bridge Bents," *Journal of Bridge Engineering ASCE*, **16**(3): 328–339.

ElGawady MA and Dawood HM (2012), "Analysis of Segmental Piers Consisted of Concrete Filled FRP Tubes," *Engineering Structures*, **38**: 142–152.

Guerrini G, Restrepo JI, Massari M and Vervelidis A (2015), "Seismic Behavior of Posttensioned Self-Centering Precast Concrete Dual-Shell Steel Columns," *Journal of Structural Engineering*, **141**(4): 04014115.

Han Q, Du XL, Liu JB, Li ZX, Li LY and Zhao JF (2009), "Seismic Damage of Highway Bridges During the 2008 Wenchuan Earthquake," *Earthquake Engineering and Engineering Vibration*, **8**(2): 263–273.

Han Q, Jia ZL, Xu K, Zhou YL and Du XL (2019), "Hysteretic Behavior Investigation of Self-Centering Double-Column Rocking Piers for Seismic Resilience," *Engineering Structures*, **188**: 218–232.

Hewes JT (2002), *Seismic Design and Performance of Precast Concrete Segmental Bridge Columns*, California: University of California, San Diego, USA.

Ichikawa S, Matsuzaki H, Moustafa A, ElGawady MA and Kawashima K (2016), "Seismic-Resistant Bridge Columns with Ultrahigh-Performance Concrete Segments," *Journal of Bridge Engineering ASCE*, **21**(9): 04016049.

Kam WY, Pampanin S, Palermo A and Carr AJ (2010), "Self-Centering Structural Systems with Combination of Hysteretic and Viscous Energy Dissipations," *Earthquake Engineering & Structural Dynamics*, **39**(10): 1083–108.

Lee WK and Billington SL (2010), "Modeling Residual Displacements of Concrete Bridge Columns Under Earthquake Loads Using Fiber Elements," *Journal of Bridge Engineering*, **15**(3): 240–249.

Li X, Lv HL, Zhang GC and Ding BD (2015), "Seismic Behavior of Replaceable Steel Truss Coupling Beams with Buckling Restrained Webs," *Journal of Constructional Steel Research*, **104**(1): 167–176.

Li X, Xiao Y, Xu YM, Lu J, Ding BD and Zhou T (2020), "Structural Behavior of Double-CFT-Pile Foundations Under Cyclic Loads," *Soil Dynamics and Earthquake Engineering*, **128**: 105863.

Marriott D, Pampanin S and Palermo A (2011), "Biaxial Testing of Unbonded Post-Tensioned Rocking Bridge Piers with External Replaceable Dissipaters," *Earthquake Engineering & Structural Dynamics*, **40**(15): 1723–1741.

Moustafa A and ElGawady MA (2020), "Performance of Double Skin FRP-Concrete Steel Self-Centered Segmental Bridge Piers Subjected to Forward-Directivity Near-Fault Ground Motion," *Engineering structures*, **197**: 109335.

OpenSees Command Manual (2020), https://opensees.berkeley.edu/wiki/index.php/Command_ Manual.

Ou YC, Chiewanichakorn M, Aref AJ and Lee GC (2007), "Seismic Performance of Segmental Precast Unbonded Posttensioned Concrete Bridge Columns," *Journal of Structural Engineering*, **133**(11): 1636–1647.

Schexnayder C, Alarcón LF, Antillo ED, Morales BC and Lopez M (2014), "Observations on Bridge Performance During the Chilean Earthquake of 2010," *Journal of Construction Engineering and Management*, **140**(4): B4013001.

Scott BD, Park R and Priestley MJN (1982), "Stress-Strain Behavior of Concrete Confined by Overlapping Hoops at Low and High Strain Rates," *ACI Journal*, **79**(1): 13–27.

Takada S, Okimura T and Lee TY (1995), Seismic Motion and Damage Characteristics. Tokyo: Preliminary Report on the Great Hanshin Earthquake, Japan Society of Civil Engineers, Tokyo, Japan.

Tong T, Zhuo WD, Jiang XF, Lei HP and Liu Z (2019), "Research on Seismic Resilience of Prestressed Precast Segmental Bridge Piers Reinforced with High-Strength Bars Through Experimental Testing and Numerical Modelling," *Engineering Structures*, **197**: 109335.

Transportation Research Board (2003), *Prefabricated Bridge Elements and Systems to limit Traffic Disruption During Construction*, *NCHRP Synthesis 324*, Washington, DC: National Research Council, USA.

Trono W, Jen G, Panagiotou M, Schoettler M and Ostertag CP (2015), "Seismic Response of a Damage-Resistant Recentering Posttensioned-HYFRC Bridge Column," *Journal of Bridge Engineering ASCE*, **20**(7): 04014096.

Wang JC, Ou YC, Chang KC and Lee GC (2008), "Large-Scale Seismic Tests of Tall Concrete Bridge Columns with Precast Segmental Construction," *Earthquake Engineering & Structural Dynamics*, **37**: 1449–1465.

Wang Z, Wang JQ, Tang YC, Liu TX, Gao YJ and Zhang J (2018), "Seismic Behavior of Precast Segmental UHPC Bridge Columns with Replaceable External Cover Plates and Internal Dissipaters," *Engineering Structures*, **177**(2018): 540–555.

Xia XS, Wu SW, Shi J, Jia JF, Chen XC and Ma HJ (2020a), "Seismic Response of Rocking Isolated Railway Bridge Piers with Sacrificial Components," *Earthquake Engineering and Engineering Vibration*, **19**(4): 1005–1015.

Xia ZH, Ge JP, Li YQ and Qiu FQ (2020b), "Shake Table Study on Precast Segmental Concrete Double-Column Piers," *Earthquake Engineering and Engineering Vibration*, **19**(3): 705–723.

Xia ZH, Lin SS, He YB, Ge JP and Sun JL (2021), "Seismic Performance of Precast Bridge Columns Connected with Grouted Corrugated-Metal Duct Through Biaxial Quasi-Static Experiment and Modeling," *Earthquake Engineering and Engineering Vibration*, **20**(3): 747–770.

Xin LF, Li XZ, Fu PY and Mu D (2022), "Seismic Behavior of Precast Segmental Column Bridges Under Near-Fault Forward-Directivity Ground Motions," *Earthquake Engineering and Engineering Vibration*, **21**(2): 559–571.

Yamashita R and Sanders D (2009), "Seismic Performance of Precast Unbonded Prestressed Concrete Columns," *ACI Structural Journal*, **106**(6): 821–830.

Yang C and Okumus P (2017), "Ultrahigh-Performance Concrete for Posttensioned Precast Bridge Piers for Seismic Resilience," *Journal of Structural Engineering*, **143**(12): 04017161.

Zhang D, Li N, Li ZX and Xie LL (2020a), "Seismic Performance of Bridge with Unbonded Posttensioned Self-Centering Segmented Concrete Filled Steel Tube Columns: An Underwater Shaking Table Test," *Soil Dynamics and Earthquake Engineering*, **138**: 106350.

Zhang Y, Tabandeh A, Ma Y and Gardoni P (2020b), "Seismic Performance of Precast Segmental Bridge Columns Repaired with CFRP Wraps," *Composite Structures*, **243**: 112218.

Zhou YL, Han Q, Du XL and Jia ZL (2019), "Shaking Table Tests of Post-Tensioned Rocking Bridge with Double-Column Bents," *Journal of Bridge Engineering*, **24**(8): 04019080.